**P2.4**

# SIERRA ROTORS:
# A COMPARATIVE STUDY OF THREE MOUNTAIN WAVE AND ROTOR EVENTS

Vanda Grubišić*and Brian J. Billings
Desert Research Institute, Reno, NV

## 1. INTRODUCTION

The Sierra Rotors Project (SRP) was the first, exploratory phase of a coordinated effort to study mountain waves, rotors, and the attendant phenomena in complex terrain, in preparation for the recently completed second phase, the Terrain-induced Rotor Experiment (T-REX, Grubišić et al. 2004). More information on SRP and its instrumentation is given in Grubišić and Xiao (2006). A total of sixteen Intensive Observing Periods (IOPs) were conducted during SRP, with the individual IOP duration ranging from 12 to 96 hours. Three of these IOPs with strong visual evidence of wave and rotors are highlighted in this paper: IOPs 8, 14, and 16.

All of these events featured single crest wave clouds which formed over Owens Valley. In IOPs 8 and 14, the cloud had a substantial along-valley extent as compared with the drier IOP 16 (Fig. 1, left). However, the wave cloud in IOP 8 appears optically thicker and lower in elevation than in IOP 14. In each event, the mountain wave is accompanied by large lenticular clouds which could be observed from the valley floor (Fig. 1, right). In IOPs 8 and 14, a line of cumulus is located underneath the leading edge of the lenticular, in the updraft of the rotor circulation. While in IOP 16 small patches of cloud were observed in the same area, the well-organized cloud formation seen in the other two cases was absent.

## 2. OBSERVATIONS AND NUMERICAL SIMULATIONS

IOP 8 was a 48 hour event from 18 UTC 24 March to 18 UTC 26 March, with a core 24 hour observing period from 12 UTC 25 March to 12 UTC 26 March. IOP 14 was 21 hours long from 12 UTC 20 April to 09 UTC 21 April, while IOP 16 was an 18 hour event from 18 UTC 28 April to 12 UTC 29 April. The SRP observations used in the analysis of these events consist primarily of surface network observations and upstream rawinsonde soundings. More information on wind profiler observations during SRP is given in Cohn et al. (2006). During each IOP, upstream soundings were provided by NCAR's Mobile GPS Advanced Upper-air Sounding System (MGAUS). MGAUS was located at Fresno for IOPs 8 and 14 and at Madera ($\approx$30 km NE of Fresno) for IOP 16.

High-resolution (333 m) numerical simulations were preformed using the Naval Research Laboratory's Coupled Ocean/Atmosphere Mesoscale Prediction System (COAMPS$^{TM}$). The model setup for all three cases was identical with the exception of the simulation period and length. Five nested domains, sixty vertical sigma levels with variable spacing (finer near the surface), and a full set of model physics were used. Lateral boundary conditions were specified using NOGAPS forecast fields, while the initial fields were created by blending the previous 12-hour COAMPS forecast with the NOGAPS analysis and synoptic observations. More detailed information on the numerical simulations is given in Grubišić and Billings (2006).

## 3. IOP OVERVIEWS

### 3.1 *Synoptic Overview*

Holmboe and Klieforth (1957) found that strong mountain wave activity in Owens Valley is associated with: i) strong westerly flow across the Sierra Nevada and ii) a cold front or an occluded front approaching the valley. During IOP 8 (Fig. 2, left) and IOP 14 (not shown), an occluded cyclone was located off the WA-BC coast with the point of occlusion passing through the Columbia Basin of Washington at some point. Trailing cold fronts extended south and southwestward through Oregon and northern California into the Pacific Ocean. In IOP 8, the 700 hPa wind was mostly SW, which is oriented approximately normal to the Sierra Nevada crestline. In IOP 14, the crest level flow was NW throughout the event. Also, the surface low and cold front in IOP 8 would eventually move onshore and pass over Owens Valley near the end of the core IOP. In IOP 14, the surface front retrograded offshore, where it alternately strengthened and weakened throughout the wave event. This type of synoptic environment characterizes the majority of cases from Holmboe and Klieforth (1957).

During IOP 16 (Fig. 2, right), conditions favorable for mountain wave activity formed in a different manner. Instead of a cyclone, a large amplitude ridge was located off the Pacific Northwest. The strong westerlies over Owens Valley resulted from a cutoff low, which dropped southward along the east side of the ridge, turning the flow to WNW for a short period of time. The surface cold front did not approach Owens Valley from the Pacific, but instead traveled toward the valley from the northeast, originating with a surface cyclone located in northern Minnesota. While the synoptic environment in this case differed from the other two cases, the underlying ingredients identified by Holmboe and Klieforth (1957) are still present.

The progressive weather systems in IOPs 8 and 16 resulted in changes in the upstream vertical structure during the course of the event, which subsequently resulted in changes in the character of the wave propagation. Due to the quasi-stationary system in IOP 14, the upstream profile was in a similar state throughout the event, as was the wave activity in Owens Valley. The upstream struc-

---

[*] *Corresponding author address:* Dr. Vanda Grubišić, Division of Atmospheric Sciences, Desert Research Institute, Reno, NV 89512; e-mail: Vanda.Grubisic@dri.edu

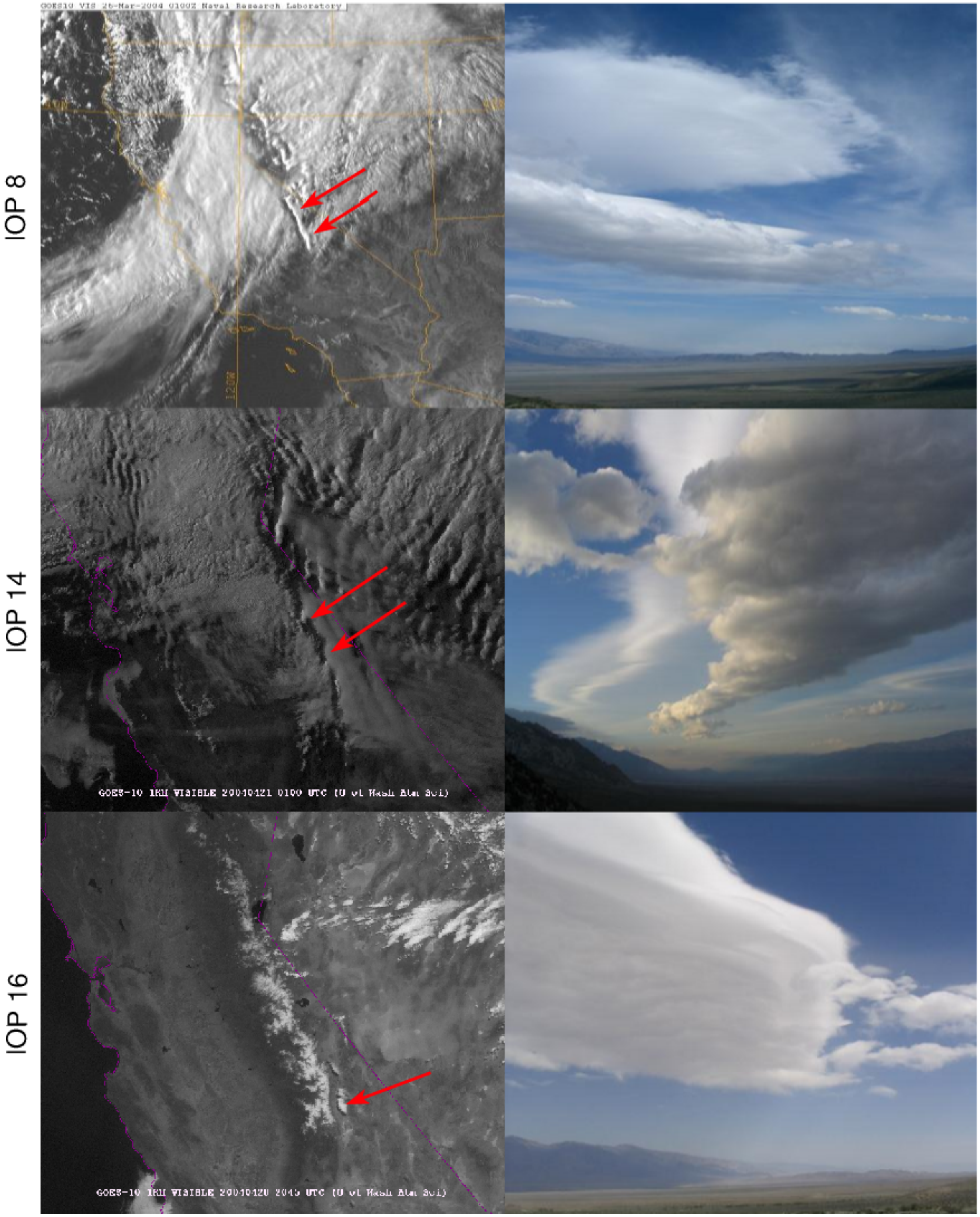

FIG. 1: Left: GOES-10 1 km visible satellite images from IOP 8 at 01 UTC March 26 (top), IOP 14 at 01 UTC April 21 (middle), and IOP 16 at 2045 UTC April 28 (bottom). Right: Photographs from Owens Valley from (top) IOP 8 at 2330 UTC March 25, looking south from west of Independence (by Vanda Grubišić), (middle) IOP 14 at 02 UTC 21 April, looking north from west of Lone Pine, and (bottom) IOP 16 at 21 UTC 28 April, looking south from west of Independence (both by Alex Reinecke).

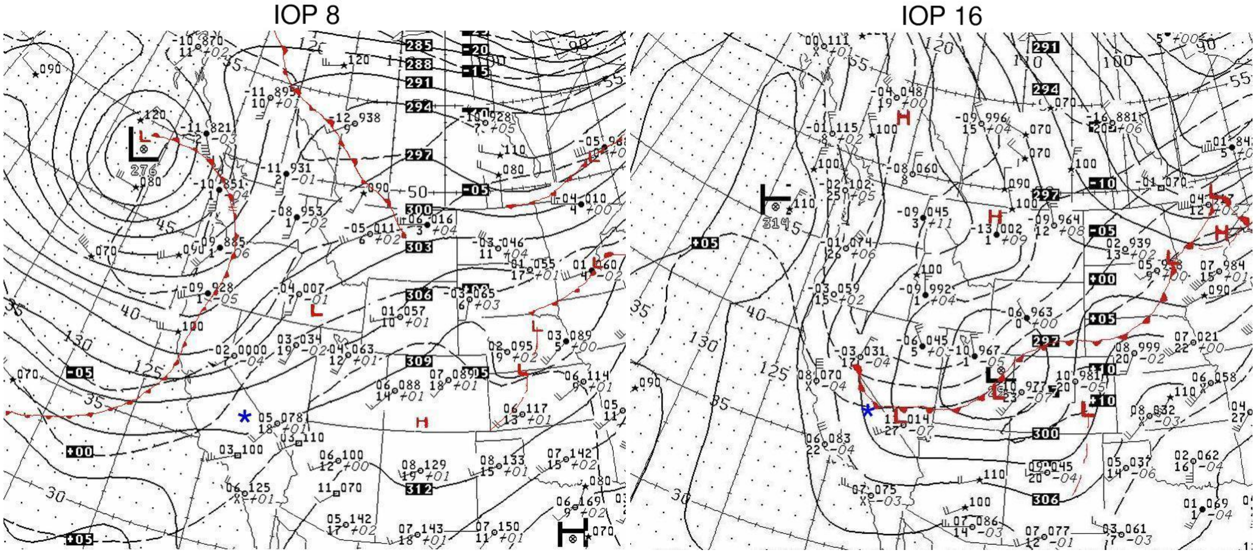

FIG. 2: 700 hPa observations and analysis (black) and Hydrometeorological Prediction Center surface fronts and pressure centers (red) for IOP 8 at 00 UTC 26 March 2004 (left) and IOP 16 at 00 UTC 29 April 2004 (right). (From National Climatic Data Center.) Independence is marked by blue stars.

ture in these events and the effect on the downstream wave activity will be discussed further in section 5.

### 3.2 *Temporal Evolution: Surface Winds*

Observations by the DRI surface mesonetwork during SRP reveal a strong diurnal component of flow variability, with the waves, rotors, and downslope flow strength reaching a maximum in the late afternoon to early evening hours. Figure 3 shows the time series of surface observations from AWS station 4 (see Grubišić and Xiao 2006) covering the core observing period of IOP 8 and the full duration of IOPs 14 and 16. During the early morning hours, the winds are relatively light and northerly, which is consistent with a downvalley flow at this station. By the mid-morning hours, the wind has reversed direction to a southerly, upvalley flow. (Stations further up the valley's western slope show an easterly, upslope flow.) In IOPs 8 and 14, there is a sharp transition to strong westerly flow between 21-22 UTC (13-14 PST). During IOP 16, this transition occurs earlier, at approximately 18 UTC (10 PST). In the early evening hours, the wind gains more of a northerly component and eventually decreases in speed, but remains relatively strong.

While IOP 8 contains a better defined thermal circulation period (possibly due to a more favorable synoptic pressure gradient and the early onset of westerlies in IOP 16), the most significant difference in the IOP 8 time series occurs at the height of the westerly wind event. At 03 UTC, there is an abrupt shift to easterly flow and a decrease in wind speed. Wind speeds also decrease at stations further up the slope, but the flow remains westerly. This appears to represent the signature of the lower half of the rotor circulation extending down to the valley floor. While roll clouds were observed during IOP 14, no reversed flow was observed by the surface network. Re-

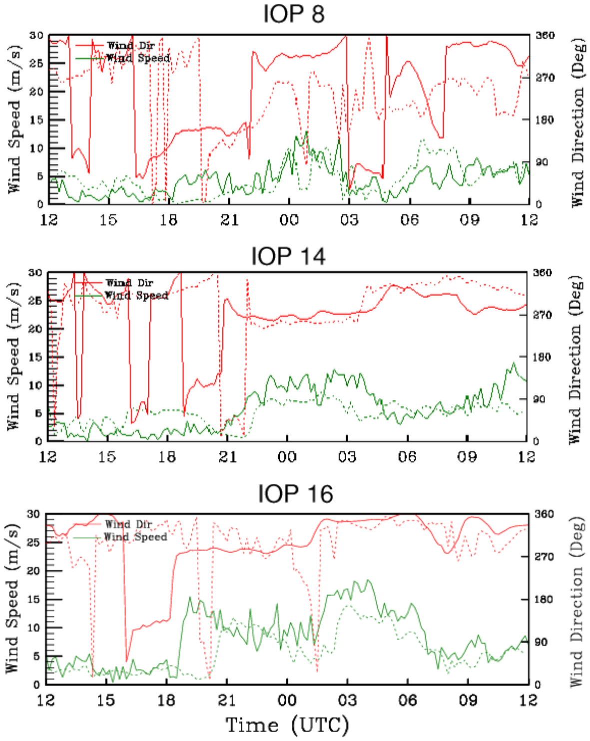

FIG. 3: Time series plots of observed (solid) and simulated (dashed) wind speed and direction at station 4 of the ground network during IOP 8 at 25-26 March (top), IOP 14 at 20-21 April (middle), and IOP 16 at 28-29 April (bottom). UTC = PST + 8 hours.

versed flow is also absent from the time series for IOP 16, though the limited western extent of the network would not capture a reversed flow that occurred far up the lee slopes. During IOP 16, AWS station 1 did record the highest wind gust of the experiment ($> 36.5$ m s$^{-1}$) during the period of strong westerlies.

Figure 3 also shows the COAMPS simulated winds at AWS station 4 during each IOP. The model is able to reproduce many features of the diurnal evolution with a slight temporal lag, including light northerlies during the early morning, the sharp transition to strong westerlies, and moderate northerlies into the evening. It also captures the southerly flow during IOP 8 (where the thermal circulation was best defined), but not in IOPs 14 and 16. The simulation does not produce the reversed flow at the same time as observed in IOP 8, but there is a brief spike of easterlies at 0050 UTC (1650 LST). The IOP 16 simulation contains two similar spikes of reversed flow that are not seen in the observations.

## 4. MOUNTAIN WAVE AND ROTOR ACTIVITY

### 4.1 *Vertical Structure*

Vertical cross-sections from the COAMPS simulations provide the best visualization of the mountain wave and rotor structure. Figure 4 shows such cross-sections passing directly over AWS station 4. In each IOP, there is a large amplitude, trapped lee wave to the lee of the Sierra Nevada with a rotor zone underneath the first wave crest. The areas of rotor activity show a reversed cross-valley wind component, near vertical isentropes on the leading edge of the updraft, indicating strong vertical mixing, and large values of turbulent kinetic energy (TKE) on the top and leading edge of the rotor circulation.

The lee wave wavelength in the IOP 8 simulation ranges from approximately 11 to 28 km. Figure 4 (top) shows the wave at a time near the core IOP's maximum wavelength, one full wavelength spanning the width of the valley. The wave crest and rotor zone are positioned over the center of the valley, which is consistent with the wind and pressure patterns observed by the surface network. On the other hand, shorter wavelengths ($\approx$10 km) were present in IOP 14 throughout the event. Figure 4 (middle) shows that the wave crest and rotor zone are located further up the slope (near AWS station 2), which again is consistent with the observed pressure patterns and wind speeds (not shown). As in IOP 8, significant variability in wavelength was simulated in IOP 16. The cross-section in Fig. 4 (bottom) shows a wavelength in between those in IOP 8 and 14. Waves with longer wavelengths without rotors were simulated at this location later in the day, and longer wavelengths with very turbulent rotor zones were simulated further north, again later in the day.

### 4.2 *Horizontal Structure*

While the DRI mesonetwork is effective at capturing episodes of strong westerly winds (Grubišić and Xiao 2006), interpreting the source of these westerlies can be difficult. The high-resolution numerical simulations can provide some insight into the AWS observations. Figure 5

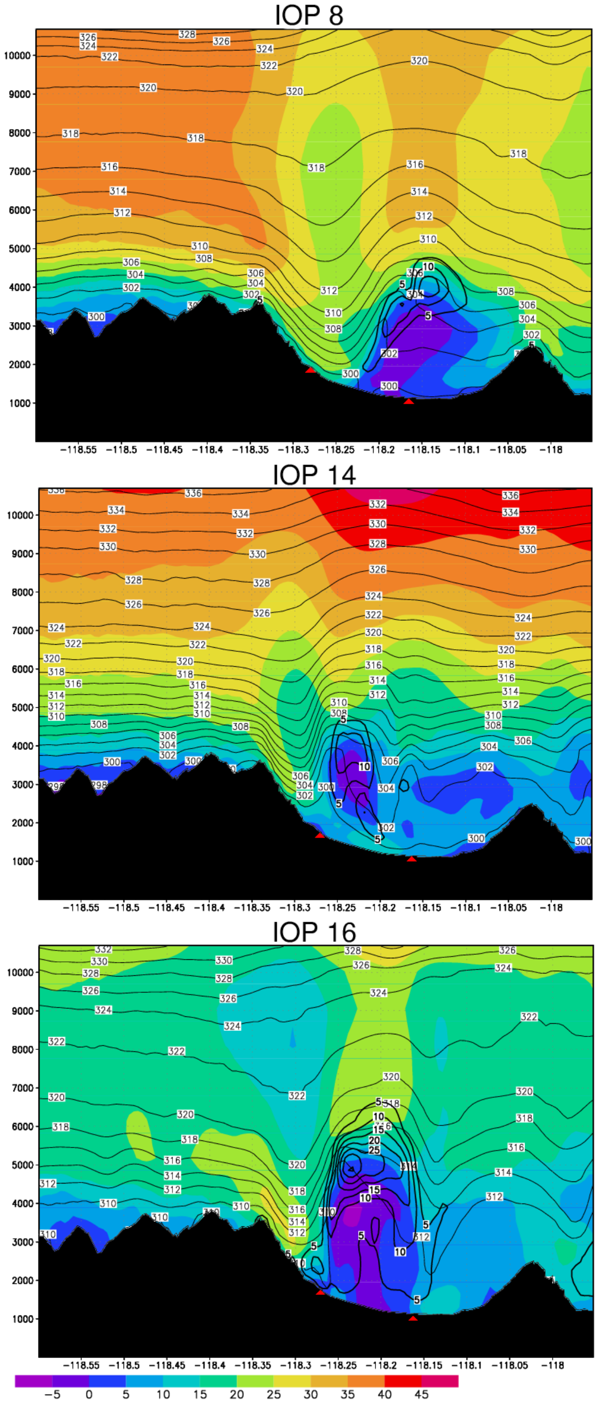

FIG. 4: Vertical cross-section (shown in Fig. 5) of isentropes (K), cross-valley wind speed (m s$^{-1}$, color shading), and TKE (m$^2$ s$^{-1}$) for IOP 8 at 04 UTC 26 March (top), IOP 14 at 03 UTC 21 April (middle), and IOP 16 at 21 UTC 28 April (bottom). The red triangles mark the location of DRI stations 1 and 4.

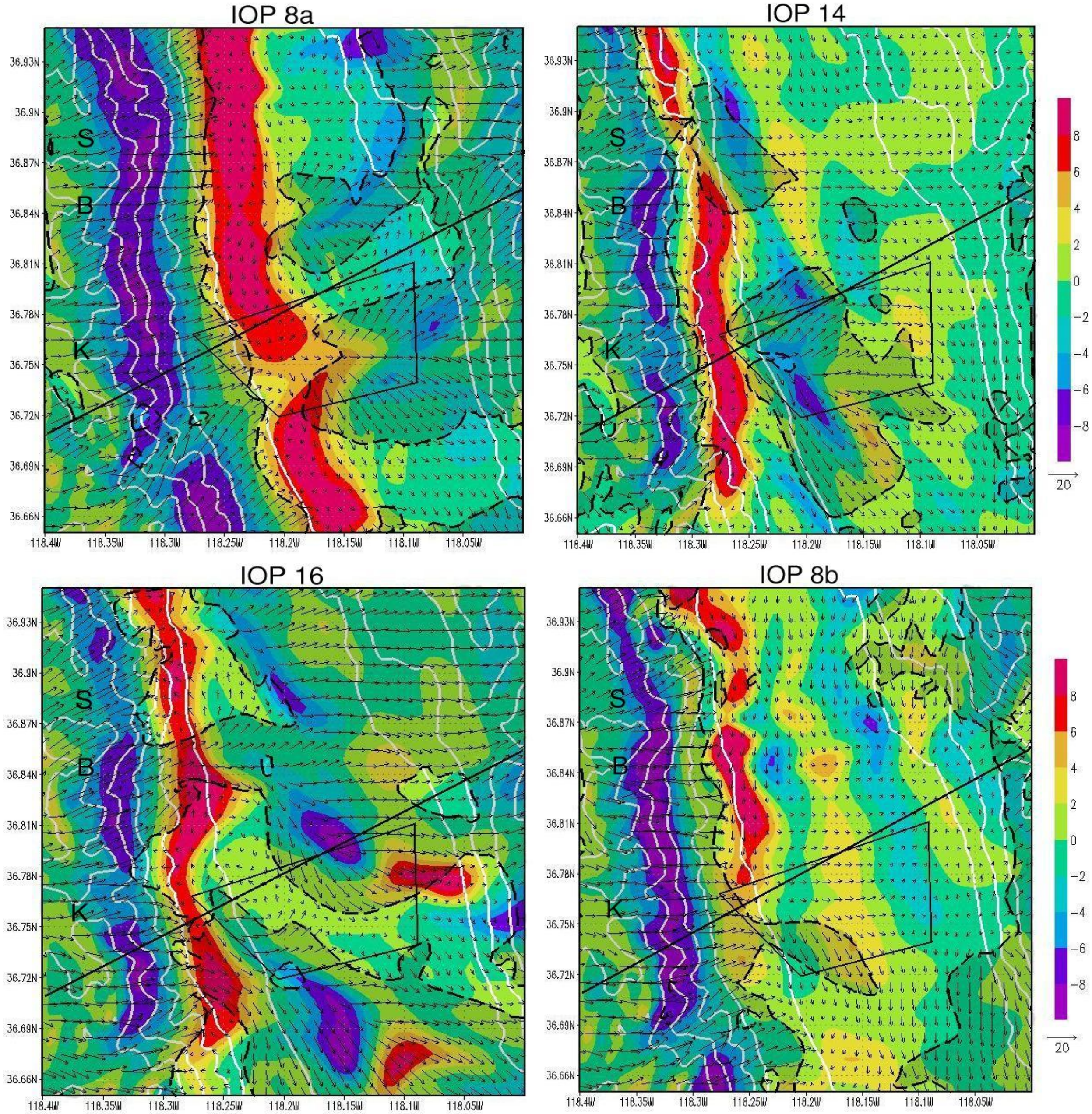

Fig. 5: Terrain (white contours), vertical velocity at 4 km (color shading), and horizontal wind vectors along the 5 m sigma surface for IOP 8 (top left), IOP 14 (top right), and IOP 16 (bottom left). Times are the same as in Fig. 4. Horizontal wind speeds of $> 6$ m s$^{-1}$ are contoured in black (dashed). Also shown are the area covered by the DRI surface network (trapezoid) and the cross-section shown in Fig. 4 (thick solid line). The same analysis for IOP 8 at 14 UTC 26 March 2004 (bottom right).

shows the wind field along the model's lowest sigma surface during periods of well-defined rotor circulations (see section 4.1). In these horizontal cross-sections, strong westerlies appear as a continuous band of downslope winds, and as gap jets. Downslope winds extend down to the base of the mountain wave trough, up to the leading edge of the wave updraft. These winds penetrate into the valley to various degrees depending on the horizontal wavelength and the preexisting flow and thermal structure in the valley. At the times shown in Fig. 5, the simulated downslope winds penetrated into the western end of the network during IOP 8, but not during IOPs 14 or 16. This agrees with mesonet observations, except for the fact that strong westerlies were being observed by this time in IOP 16. (The simulated downslope winds would reach the western edge of the network a few hours later.)

While the strong downslope winds extend to the base of the mountain wave trough, from the wave trough to the wave crest, the winds are typically much weaker, or even reversed. On the other side of the crest, strong westerlies associated with the pressure-driven circulations of a large-amplitude mountain wave (Fig. 6) can be seen if the wave amplitude is large enough and the horizontal wavelength is sufficiently short for the second wave trough to be located over the valley. This is seen in Fig. 5 for IOPs 8a and 14.

Extending from the band of downslope winds further into the valley are gap jets, which can be traced back to major passes in the Sierra Nevada, such as Kearsarge Pass (≈36.75° N), Baxter Pass (≈36.84° N), and Sawmill Pass (≈36.88° N). In IOPs 8 and 14, these gap jets seem to disrupt the mountain wave and rotor structure. [In Fig. 5 (top left), there was a gap jet a few hours earlier at the location of the break in the strongest updraft.] However, this does not seem true in IOP 16. In fact, gap jets during this case seem to be associated with narrow bands of strong wave activity which extend across the valley.

Another variability involving the gap jets is that the strongest jet originates from a different pass at different times and among various IOPs. At the time periods shown in Fig. 5, the strongest jet is from Kearsarge pass in IOP 8, from Sawmill pass in IOP 14, and from Baxter pass in IOP 16. Earlier in IOP 14, the jets were equally strong from all three passes, and in other IOPs, the relative strength of each gap jet varied throughout the evolution of the event.

Finally, if instead of a trapped lee wave, the wave response is that of a vertically propagating wave, strong westerlies can be channeled between the surface and wave breaking aloft. Strong vertical propagation and wave breaking was simulated toward the end of the core period of IOP 8. The horizontal view of the downslope winds in this case is illustrated in Fig. 5 (bottom right), showing westerlies that extend beyond the base of the trough into the valley, particularly over the area of the surface network. The cases presented here are a more moderate example of this type of flow, which is more significant in other SRP events. The transition between different wave propagation regimes and the vertical structure of the wave breaking aloft will be discussed next.

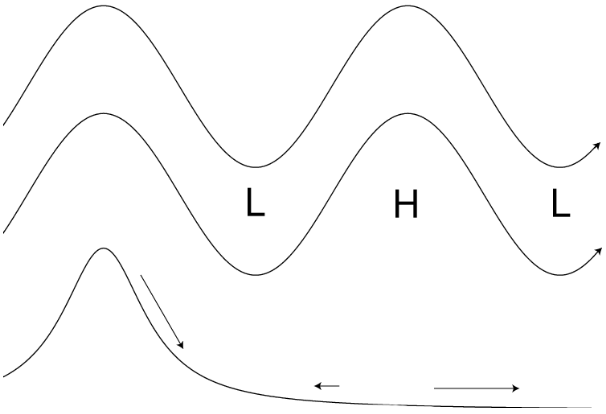

FIG. 6: Schematic diagram of large amplitude wave induced pressure and surface wind anomalies.

## 5. WAVE PROPAGATION REGIMES

As seen in section 4.1, rotors are best formed when the wave energy is trapped at low levels. There are multiple upstream conditions that can lead to this wave trapping. Vosper (2004) used a numerical model to show that an inversion at or above the height of the mountain crest could lead to rotors downstream. Also, if the wind speed rapidly increases with height accompanied with a rapid decrease of stability, wave energy will tend to be trapped at low levels (Scorer 1949). In contrast to the wave-trapping regime, when upstream stability and wind are more uniform with height and no significant inversions are present, waves will be able to propagate more freely in the vertical. At certain times in the time evolution of IOPs described here, stronger vertical wave penetration was exhibited.

In IOP 14, upstream soundings near the beginning and end of the event (Fig. 7, middle) both show strong wind shear and a significant stability between 5-7 km. (This wind shear can be seen in Fig. 4 as well.) Consequently, downstream model cross-sections show wave energy being trapped at low levels throughout the event. On the other hand, IOPs 8 and 16 involve transitions in the upstream structure, with and without inversions, and the downstream vertical wave propagation. Prior to the frontal passage in IOP 8, the upstream soundings show strong wind shear and a distinct two-layer stability profile with more unstable air aloft (Fig. 7, top). After frontal passage (≈09 UTC 26 March), both the stability and wind speed profile become more uniform with height. (Missing data around 03 UTC is the result of freezing rain associated with the approaching cold front.) Figure 8 (left) shows the downstream flow during this regime with more vertical wave propagation and wave breaking aloft (cf. Fig. 4,top). In contrast, during IOP 16, the vertical wave propagation occurs at the beginning of the event (Fig. 8,right), before the cutoff low strengthens and the surface front approaches. A few hours later, stronger wind shear develops as wind speeds increase aloft, and a thin stable layer develops at 5 km (≈500 hPa). This leads to the wave trapping in the valley, which intensifies as the vertical shear continues to increase (Fig. 7, bottom).

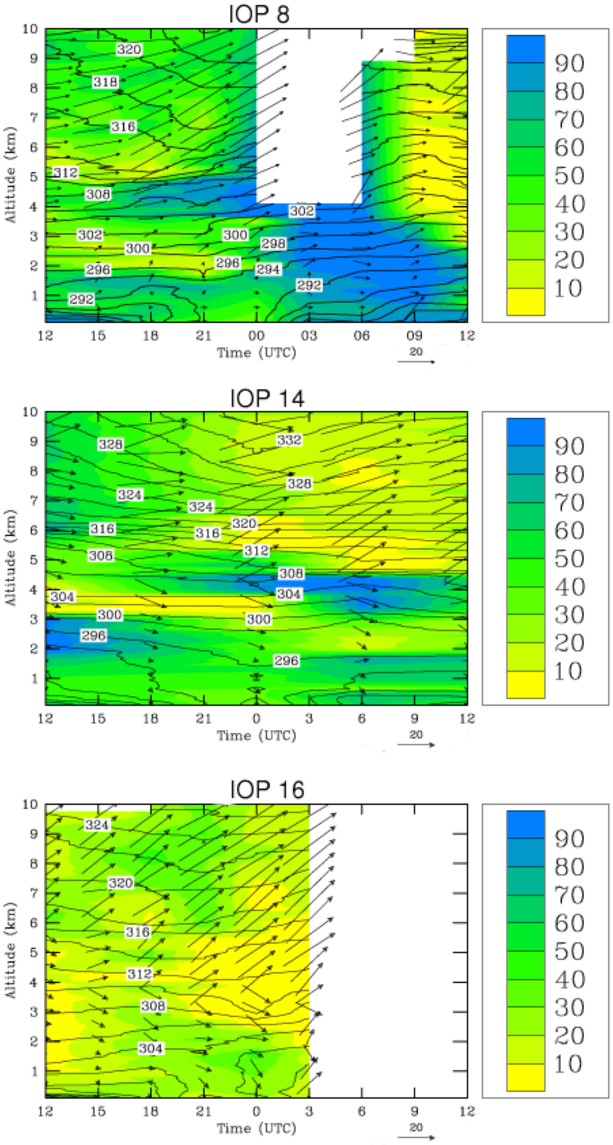

FIG. 7: Time-height diagram showing relative humidity (%, shaded), isentropes (contour interval 2K), and wind field (unit vector 20 m $s^{-1}$) from MGAUS during the 24-hour period between 12 UTC and 12 UTC for IOP 8 at 25-26 March (top), IOP14 at 20-21 April (middle), and IOP 16 at 28-29 April 2004 (bottom).

## 6. SUMMARY AND CONCLUSIONS

During the Sierra Rotors Project, three IOPs were significant for the visual evidence of wave and rotor activity in cloud formations and the strength of the winds which penetrated the valley. IOPs 8, 14, and 16 each formed under synoptic conditions characterized by strong cross-mountain flow and a pre-frontal environment. All three events featured the same diurnally varying sequence of wind regimes: light, downvalley flow during the early morning through light, upvalley and upslope flow during the mid-morning to strong westerlies at mid-day or in the afternoon. Each event featured a combination of strong downslope winds and gap jets in the surface wind field. Finally, in each event rotors formed in the presence of significant wave trapping at lower levels.

IOP 8 culminated in reversed, easterly flow observed at the surface. The waves formed in SW flow and a frontal passage occurred near the end of the core observing period. At its peak strength, the mountain wave had a long ($>$ 27 km) wavelength with the wave crest positioned over the valley center and downslope winds reaching the western edge of the mesonetwork. Strong winds also formed on the far side of the mountain wave crest and underneath vertical wave propagation and breaking which occurred after frontal passage.

IOP 14 did not feature a reversed surface flow. The waves formed in NW flow, and the cold front remained offshore. The trapped lee wave was shorter in wavelength with the first crest and downslope winds positioned further up the eastern Sierra Nevada slopes. Wave trapping remained in place throughout the event, so strong westerlies observed by the network were likely due to gap jets and pressure-driven winds downstream of the wave crest. In IOPs 8 and 14, these gap jets seemed to disrupt the mountain wave and rotor structure.

IOP 16 contained the largest surface wind gust observed during the two-month field campaign. A less common synoptic environment featured a cutoff low moving directly southward from Pacific Northwest and a cold front approaching from the northeast. As in IOP 8, a large range of wavelengths was simulated with the maximum placing the wave crest and rotor over the center of the valley. Vertical wave propagation occurred at the beginning of the event, before the upper jet and surface front approached the valley. Unlike in IOPs 8 and 14, the gap jets in this case seemed to drive the strongest vertical motions. The recently completed Terrain-induced Rotor Experiment (T-REX, Grubišić et al. 2004) has acquired more detailed observations of additional mountain wave and rotor events that will be used in the future to expand the analysis and conclusions presented here.

## ACKNOWLEDGMENTS

The high-resolution real-data COAMPS runs were carried out on the Mesoscale Dynamics and Modeling Laboratory's 68-processor Sierra cluster at DRI funded

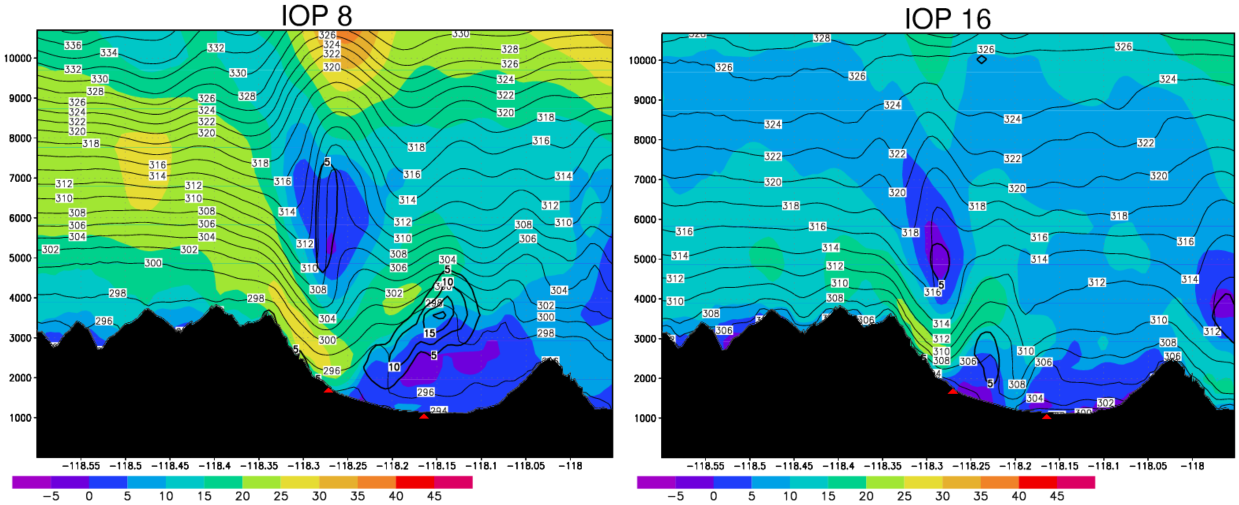

FIG. 8: As in Fig. 4, but for IOP 8 at 14 UTC 26 March (left) and IOP 16 at 12 UTC 28 April (right).

by the NSF grant ATM-0116666. This research was supported in part by the NSF grant ATM-0242886. SRP was a joint effort between DRI, NRL, and the University of Washington. We thank Dale Durran, Jim Doyle, Qingfang Jiang, Steven Cohn, and Bill Brown for their efforts during the SRP field phase and Ming Xiao for the analysis of the surface observations.

## REFERENCES

Cohn, S. A., W. O. J. Brown, V. Grubišić, V., and B. J. Billings, 2006: The signature of waves and rotors in wind profiler observations. *Online Preprints: 12th Conference on Mountain Meteorology.* Amer. Meteor. Soc., Paper **P2.7**

Grubišić, V., and M. Xiao, 2006: Climatology of westerly wind events in the lee of the Sierra Nevada. *Online Preprints: 12th Conference on Mountain Meteorology.* Amer. Meteor. Soc., Paper **P2.8**

——-, and B. J. Billings, 2006: The intense lee-wave rotor event of Sierra Rotors IOP 8. Manuscript submitted to *J. Atmos. Sci.*

——-, J. D. Doyle, J. Kuettner, G. S. Poulos, and C. D. Whiteman, 2004: Terrain-induced Rotor Experiment (T-REX) Overview Document and Experiment Design. 72 pp. www.joss.ucar.edu/trex/documents/TREX_SOD.pdf

Holmboe, J. R., and H. Klieforth, 1957: Investigation of mountain lee waves and the airflow over the Sierra Nevada. Final Report. Department of Meteorology, UCLA, Contract AF 19(604)-728, 283 pp.

Scorer, R. S., 1949: Theory of lee waves of mountains. *Q. J. R. Meteorol. Soc.,* **75,** 41-56.

Vosper, S. B., 2004: Inversion effects on mountain lee waves. *Q. J. R. Meteorol. Soc.,* **130,** 1723-1748.